PCCP

PAPER

View Article Online
View Journal | View Issue

Cite this: *Phys. Chem. Chem. Phys.*, 2016, **18**, 26184

Carrier transport behaviors depending on the two orthogonally directional energy bands in the ZnO nanofilm affected by oxygen plasma†

Cheolmin Park,[ab] Seung-Mo Lee[ab] and Won Seok Chang*[ab]

Received 23rd June 2016,
Accepted 30th August 2016

DOI: 10.1039/c6cp04391g

www.rsc.org/pccp

An oxygen plasma treatment of ZnO nanostructures has frequently been used for obtaining a desired optoelectrical property. Nevertheless, a detailed study regarding carrier transport behaviors affected by the plasma has scarcely been managed, especially in the thin film structure, owing to its more complex physics than those of a one-dimensional nanostructure. Herein, we demonstrate an analysis of carrier transport behaviors on an oxygen plasma-treated ZnO nanofilm (50 nm thick) on a SiO_2/Si substrate. By comparison with the as-grown sample, we observed drastic changes in carrier transport behavior according to the short exposure times of 30 s and 60 s. The plasma effect leading to the distinction was confirmed to originate from the bombardment of energetic ions near the surface and the diffusion of various oxygen ions and radicals into the host. The mechanism of the resulting carrier transport was comprehended through the revelation of two orthogonally directional energy band structures (surface band bending in the surface layer and localized energy bending at the grain boundary). Furthermore, we experimentally observed that the increased electrical barrier of the grain boundary, due to negatively absorbed oxygen ions, could be helpful in impeding persistent photoconductivity and in reducing dark current.

1. Introduction

The n-type semiconducting zinc oxide (ZnO) nanostructures have been extensively researched for various functional devices such as TFTs (Thin Film Transistors),[1,2] TCOs (Transparent Conductive Oxides),[3,4] ultraviolet (UV)/blue LEDs (Light-Emitting Diodes),[5] UV photodetectors,[6,7] chemical sensors[8] and pressure sensors.[9] This interest in ZnO is owing to its diverse intrinsic properties: wide band gap (E_g = 3.4 eV at room temperature) with a large exciton binding energy (60 meV), piezoelectricity, and adsorption/desorption processes in ambient air.[10] Additionally, since it can be crystallized at low temperature, flexible devices can also be fabricated with ZnO.[1,4]

However, importantly, optical and electrical properties of ZnO nanostructures can easily be affected by growth condition, size, morphology, and ambient air condition; which are mostly associated with native defects caused by non-stoichiometry such as oxygen vacancy (V_O), zinc vacancy (V_{Zn}), Zn interstitial (Zn_i), and oxygen interstitial (O_i).[10,11] Therefore, to modulate these defect states for desired properties, post-processing techniques, mainly thermal annealing and plasma treatments, have largely been studied with respect to various ZnO structures such as ultrathin film,[2,7] nanowires,[12,13] and nanorods.[14,15] Plasma treatment techniques, in particular, have several advantages over thermal annealing, such as fast-processing time, the fact they are low-temperature processes enabling application to flexible devices, low-energy consumption, and controllability with several gas species (*e.g.*, hydrogen, argon, oxygen).[12–14,16] Notably, the influence of plasma on nanostructured ZnO is particularly effective due to the large surface-to-volume ratio, which seems to promote the use of plasma in ZnO nanostructures.[12,13]

Even though a number of studies of plasma-treated ZnO have been done, exact mechanisms of carrier transport behaviors affected by plasma have rarely been reported. In particular, the investigation of ZnO nanofilms has scarcely been carried out, compared with single crystal nanostructures such as nanowires and nanorods.[17] This could be attributed to the complex physics of carrier transport because there exists a high density of grain boundary (GB), nontrivial surface defect states in ambient air, and probable quantum confinement effects in the lower part of the thin film thickness, due to the extremely small grain size.

In this study, we systematically investigated the mechanism of the carrier transport behaviors in ZnO nanofilm according to its time of exposure to oxygen plasma. We specifically employed the measurement of time-resolved photocurrent with on/off

[a] *Nano-convergence Mechanical Systems Research Division, Korea Institute of Machinery and Materials (KIMM), 156 Gajungbukno, Daejeon 305-343, Republic of Korea. E-mail: paul@kimm.re.kr*

[b] *Department of Nano-mechatronics, Korea University of Science and Technology (UST), 217 Gajeong-ro, Daejeon 305-333, Republic of Korea*

† Electronic supplementary information (ESI) available. See DOI: 10.1039/c6cp04391g

control of ultraviolet light because it provides comprehensive carrier behaviors with regard to generation and recombination processes related to carrier concentration, the electrical barrier effect of the GB, and the influence of the surface states. The observed photoresponse according to the plasma exposure time appeared as distinct curves, compared with that of an as-grown sample. With additional supporting data such as surface chemistry, crystallinity, and carrier concentration, we confirmed that the resulting carrier transport was caused by the correlation between two orthogonally directional energy bands: the localized electrical barrier of GB and the surface band bending in the surface layer.

2. Methods

2.1. Sample synthesis

The SiO_2/Si substrate was placed in an ALD (Atomic Layer Deposition) reactor (Savannah 100, Cambridge Nanotech, Inc.) and dried at 70 °C for 30 minute (min) in vacuum condition (1×10^{-2} Torr) with a steady N_2 gas stream (20 sccm). For deposition of ZnO, DEZn (diethylzinc, $Zn(C_2H_5)_2$, Sigma-Aldrich) and deionized H_2O were used as zinc and oxygen sources, respectively. To deposit an atomic layer 50 nm thick, the substrate was alternately exposed to/purged from $Zn(C_2H_5)_2$ and H_2O vapor for 250 cycles. The pulse/exposure/purge times of $Zn(C_2H_5)_2$ and H_2O were 0.1 s (s)/30 s/40 s and 0.1 s/30 s/40 s, respectively.

As-grown ZnO samples were treated respectively by oxygen plasma with exposure times of 30 s, 60 s, 90 s and 120 s, which supplied a radio-frequency (RF) power of 100 Watt. During the plasma exposure, the gas flow rate and oxygen pressure were 60 cc min^{-1} and 273 mTorr, respectively.

For photocurrent measurement, a Ti/Au layer of 3 nm/50 nm thickness was deposited on the surface of the ZnO/substrate by a thermal evaporation method (KOREAVAC, KVE-T2000) with a shadow mask having a 50 μm gap between electrodes. During the thermal evaporation process, the sample holder was water-cooled to avoid the thermal effect.

2.2. Characteristics

The thickness of a deposited ZnO nanofilm was confirmed by cross-sectional scanning electron microscopy (SEM, Hitachi, S-4800) images. The surface morphology of the samples was investigated by AFM (Atomic Force Microscopy, NT-MDT, Ntegra) with a scanning area of 1.5×1.5 μm^2. The chemical nature at the surface of the samples was measured by an X-ray photoelectron spectrometer (XPS, KRATOS, AXIS NOVA). The measured O 1s peaks were deconvoluted using OriginPro 8.6. The crystallinity was characterized using an X-ray diffractometer (XRD, Bruker, D8 Advance) with Cu Kα radiation (wavelength λ = 1.5418 Å). The two-theta range was from 30–38 degrees with a scan speed of 0.2 degree min^{-1}. Electrical properties such as conductivity, carrier concentration and mobility were obtained from Hall-effect measurements (Ecopia, HMS-5000) conducted *via* the Van der Pauw method at room temperature. During the process, the magnetic field and measuring current were 0.55 T and 1.5 mA, respectively. In a dark room, dark current and photocurrent under illumination of a 355 nm laser (CNI, DOI-UV-F-355-CW) were obtained with a sweeping bias voltage from 0 to 5 V using a high-speed source/monitor unit (Agilent Technologies, E5262A). The photoresponse time under illumination of the UV light was measured using a low-noise current preamplifier (Stanford Research Systems, SR570).

3. Results and discussion

3.1. Characteristics of the plasma-treated samples, compared with the as-grown sample

The deposition of ZnO nanofilm on a SiO_2/Si substrate was achieved using the ALD technique[18,19] at low temperature (90 °C). In order to study carrier transport behaviors resulting from the oxygen plasma effect, we first investigated the electrical properties of the plasma-treated ZnO nanofilm according to the various plasma exposure times of 30, 60, 90 and 120 s *via* Hall-effect measurement (see Fig. S1, ESI†). Through repetitive experiments, we found that there always existed maximum and minimum conductivities at the exposure times of 30 and 60 s, respectively. To establish the causes of these notable changes in conjunction with carrier transport behavior, we intensively examined the plasma-treated samples exposed for 30 and 60 s, comparing them with an as-grown sample (hereafter called the as-grown sample, the 30 s sample and the 60 s sample).

First of all, because the surface morphology of the nanostructured oxide–semiconductor affects its optoelectrical properties,[10,11] we carried out AFM measurements to confirm a probable change in surface morphology due to the plasma treatment. The average surface roughness of the as-grown sample (R_a: 1.106 nm) was clearly improved in accordance with the increasing exposure time (R_a of 30 s and 60 s: 1.048 and 0.977 nm, respectively, see Fig. S2, ESI†). However, the surface height distribution in Fig. 1(a) shows that the rate of improvement in surface roughness was higher in the later 30 s than in the early 30 s. Supposing the roughness improvement is dependent on the surface area-to-volume ratio, the observed rate shows the opposite result, which could indicate that there exists a discontinuous influence of the plasma on the ZnO nanofilm during 1 min exposure time.

It is well known that the surface morphology of ZnO nanostructures strongly influences the surface chemistry due to the morphology-dependent surface defect states and the resultant adsorbed molecules.[10,11] In other words, as mentioned before, due to the intrinsic non-stoichiometry of ZnO, it exhibits surface defects, especially dominant oxygen vacancies which play a role as donors because missing oxygen leaves free electrons.[20,21] In addition, the number of oxygen-deficient sites increases in the nanostructured ZnO due to the high surface-to-volume ratio, which induces higher electron density in the surface layer. Therefore, oxygen molecules in ambient air adsorb onto the surface by capturing free electrons, forming negatively charged oxygen ions in the surface layer. Furthermore, the surface chemical states are associated with the electrical and optical properties of ZnO nanostructures.[11] Therefore, we investigated

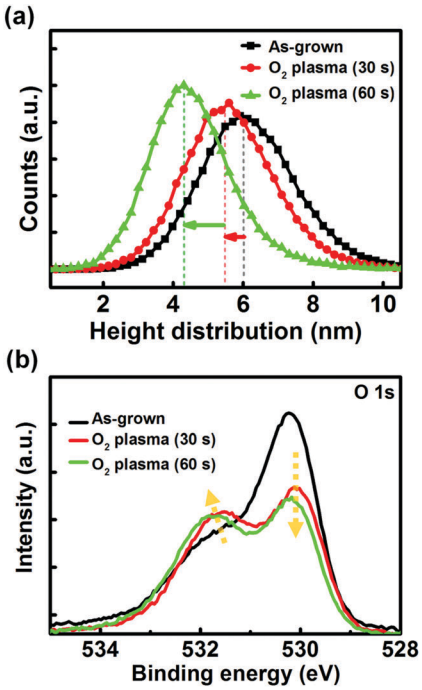

Fig. 1 Surface height distribution of (a) samples measured by AFM. The maximum peak positions (with full-width-half-maximum) of the as-grown, and the samples of 30 s and 60 s were 6.1 nm (3.17), 5.5 nm (2.97), and 4.4 nm (2.60), respectively. This indicates clearly a significant effect on surface morphology according to the time of exposure to the plasma. The surface improvement rate of the 60 s sample (the green arrow) is higher than that of the 30 s sample (the red arrow). XPS spectra (b) of the O 1s peaks with identical *y*-axis scale show the influence of the exposed time, compared with the as-grown sample. The orange dashed arrows indicate a change in peaks according to the increased expose time.

the surface chemistry using XPS measurement for the O 1s peak. Fig. 1(b) shows that the longer the exposure time to the plasma, the lower the intensity of low binding energy near 530 eV, but the higher the intensity of high binding energy near 532 eV. To investigate the XPS data in detail, the O 1s peak spectra were deconvoluted into three peaks (LP, MP, and HP; see Fig. S3, ESI†). Table 1 gives a summary of the area ratios of the three peaks. The ratio (MP)/(LP + MP + HP) of the 30 s sample, indicating the density of oxygen vacancies, was greater than that of the as-grown sample, whereas it was less in the 60 s sample. This shows that the initial exposure time (30 s) results in the breaking of the Zn–O bonds near the surface.[12,15,16] Whereas, an additional exposure time of 30 s (the 60 s sample) led to a reduced density of oxygen vacancies and increased adsorption of oxygen ions and radicals.[7] This was confirmed by the higher value of (HP)/(LP + MP + HP), representing the density of adsorbed species.

Table 1 Summary of the area ratios related to deconvoluted O 1s peaks

Samples	MP/ (LP + MP + HP)	HP/ (LP + MP + HP)	(MP + HP)/ (LP + MP + HP)
As-grown	0.199	0.277	0.476
O_2 plasma (30 s)	0.340	0.282	0.621
O_2 plasma (60 s)	0.254	0.392	0.646

Table 2 presents the Hall-effect measurement. The carrier concentration in the 30 s sample was 6.7 times higher than in the as-grown sample, with decreasing mobility. In contrast, the 60 s sample exhibited a decrease in carrier concentration similar to the level of the as-grown sample, with increasing mobility, which is well coincident with XPS data regarding the density of oxygen vacancies (MP/(LP + MP + HP)) related to the electron concentration. Regarding mobility, the oxygen-deficient sites could induce carrier trapping and scattering, which results in a decline in mobility.

The crystallinity of the whole volume was characterized by XRD measurement, as shown in Fig. 2(a). The XRD pattern indicates well (100), (002), and (101) planes of the wurtzite crystal structure. The preferential growth of the two peaks of (100) and (101) over the peak of *c*-axis (002) is attributed to deposition of ultrathin films on the amorphous substrate. The average grain size of the planes was approximately 25–35 nm, as calculated by Scherrer's equation. Note that the samples of 30 s and 60 s appeared slightly shifted to high and low angles, respectively, based on an XRD pattern of the as-grown sample. A high-angle shift means a decrease in lattice distance,[22,23] while a low-angle shift indicates in-plane stress due to elongation of the lattice of ZnO.[7] (The causes of the shifting peaks are described later.)

The contrasting characteristics of the 30 s and 60 s samples, such as the surface chemistry, electrical properties and crystallinity, compared with the as-grown sample, definitely suggests that there exists an irregular interaction between the plasma and ZnO nanofilm during the treatment exposure for 1 min. To establish the cause of the distinction and its association with carrier transport, the dark current and photocurrent were measured with sweeping bias voltages from 0 to 5 V after fabricating a metal–semiconductor–metal (MSM)-type device, as shown in the inset in Fig. 2(b). The current–voltage characteristics also presented a distinction between the samples of 30 and 60 s, which was in near accord with the previous XPS data and the Hall-effect measurement. That is, the 30 s sample has the highest dark current due to its high carrier concentration (originating from the high density of oxygen vacancies); whereas the abundant vacancies also contribute to an increase in photocurrent under UV light due to a resultant increased gain in the MSM-type device.[6,11] The 60 s sample had a slightly larger photocurrent than the as-grown sample owing to a slightly higher density of oxygen vacancies, whereas it had the lowest dark current among the samples. This could be caused by the adsorbed species acting as an electron trap and providing a stronger GB effect. (The GB effect is described in more detail later.)

Table 2 Summary of electrical properties obtained by Hall-effect measurement at room temperature

Samples	Carrier concentration (10^{19} cm^{-3})	Mobility (cm^2 V^{-1} s^{-1})	Conductivity (Ω^{-1} cm^{-1})
As-grown	7.2	1.99	22.9
O_2 plasma (30 s)	48.4	0.38	30.0
O_2 plasma (60 s)	7.8	1.46	18.3

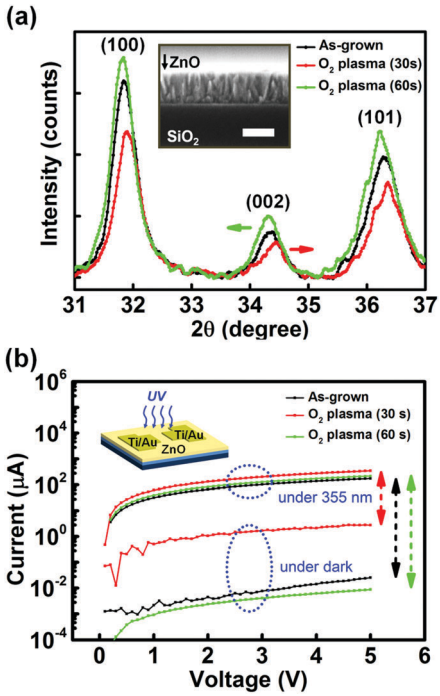

Fig. 2 XRD patterns of (a) samples: the red and green arrows indicate the high-angle shift of the 30 s sample and the low-angle shift of the 60 s sample, respectively, compared with the as-grown sample. The inset shows a cross-sectional SEM image of as-grown nanofilm on SiO_2/Si substrate (scale bar is 50 nm), which presents the boundaries of gain. The dark current and photocurrent under UV light (wavelength 355 nm, power 1.3 μW) with sweeping bias voltage from 0 to 5 V (b) were measured after fabrication of the MSM-type device (inset). The vertical dashed lines indicate the differences between dark current and photocurrent in each sample.

3.2. Physical effect of oxygen plasma on the ZnO nanofilm according to exposure time

The physical changes in the ZnO nanofilms according to the plasma exposure time are due to oxygen ion bombardment[12,15,16] and the densification effect.[7,24] Furthermore, in spite of the short exposure times, the strong reactivity generated in the ZnO nanofilm is mainly due to the high GB density, which gives rise to a large interfacial area-to-volume ratio. This is because the interfacial area acts as a reactive site for ambient molecules and furthermore provides a faster diffusion path for outside molecules than in the pure bulk. The schematic diagram in Fig. 3(a) (figures on the top line) represents the physical effects of the oxygen plasma process on the ZnO nanofilm, according to the exposure time. Originally, the surface of the as-grown sample had weak bonds such as OH bonds and adsorbed H_2O molecules because the ALD process involves water at low temperature.[25] In this condition, once the as-grown sample is exposed to plasma for 30 s, the energetic ions and radicals break the weak bonds. As a result, this causes a high density of oxygen vacancies, leading to an increase in carrier concentration in the surface layer, with brief diffusion of oxygen into the GB. The introduction of abundant oxygen-deficient sites was sufficiently confirmed by XPS, the Hall-effect measurement and the high-angle shift in XRD resulting from the decrease in lattice distance.[22,23] After that, during the additional short exposure of 30 s, the energetic oxygen ions and radicals (*e.g.*, O^+, O_2^+, and O*), along with oxygen atoms and molecules, were diffused into the host. This was enabled by their high diffusivity in oxide, even at moderate temperatures.[26] Furthermore, they

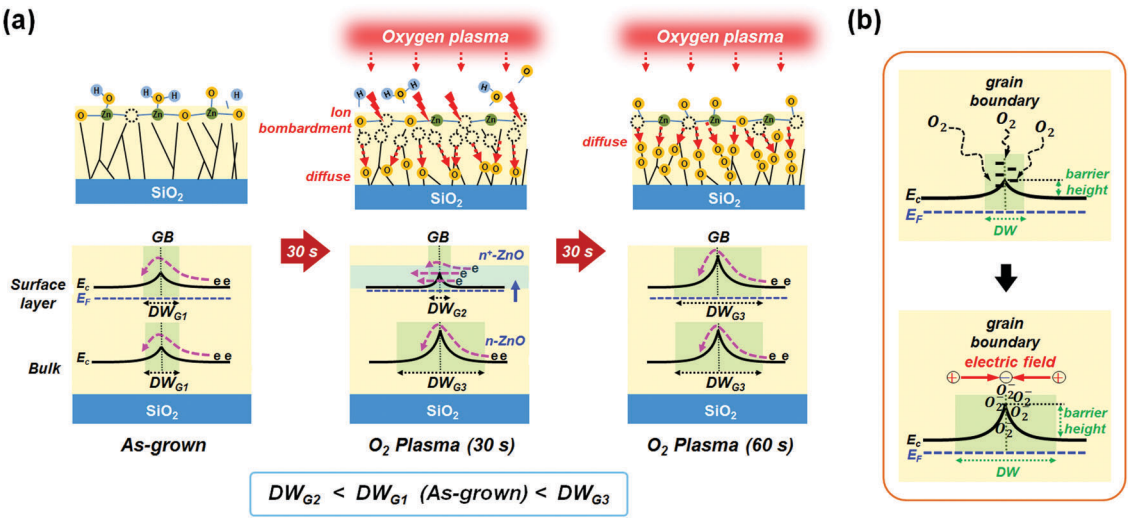

Fig. 3 Schematic diagrams regarding physical effect of oxygen plasma on the ZnO nanofilm according to exposure time. (a) Shows physical effects of oxygen plasma processes according to the exposure time of the ZnO nanofilms, with their grain boundary band structure. There exists an ion bombardment effect and diffusion during oxygen plasma exposure, as shown in the figures on the top line. The dashed circles and the red dashed arrows in the ZnO nanofilm indicate oxygen-deficient sites and the diffusion of oxygen ions and radicals, respectively. The figures on the bottom row show that energy band structures (with regard to grain boundary) are affected by the oxygen plasma. The high density of oxygen-deficient sites, leading to an increase in the Fermi-level in the surface layer of the 30 s sample, results in a narrowed depletion width (DW_{G2}) of the grain boundary, while the 60 s sample has a wide depletion width (DW_{G3}) because of the fully adsorbed oxygen at the grain boundary over the whole volume of the ZnO nanofilm. (b) Shows energy band structures at the GB without and with the adsorbed oxygen molecules. The GB has defect states, with regard to oxygen vacancies, where the oxygen molecules in the air adsorb by capturing free electrons. The negatively charged oxygen ions at GB induce an electric field, which increases its depletion width.

easily pass through GB on a fast path because the diffusion rate at the grain boundary can be almost three to four orders of magnitude greater than in doped and pure ZnO.[27] In other words, the diffusion strongly increases the electrical barrier of GB by formation of adsorbed negative oxygen ions (O^{2-}) at the GB, as shown in Fig. 3(b).[12,13] Overall, these activities cause a densification effect in the bulk and the surface layer, as proved by XPS data and XRD data. That is, in the case of XRD data, the low-angle shift indicating elongation of the lattice of ZnO[7] in the 60 s sample is due to the densification effect. These resulting physical phenomena have a decisive effect on carrier transport behavior. In the surface layer of the 30 s sample (figures on the bottom line), the generation of abundant oxygen-deficient sites on the whole surface layer raises the Fermi-level and reduces the electrical barrier of GB, while the depletion width of GB in the bulk is slightly widened due to the brief diffusion. Therefore, because the resistivity could be higher in the bulk than in the surface layer, most carriers could flow in the surface layer, as shown in the transparent blue box in the figure. In the case of the 60 s sample, by a nearly sufficient diffusion of oxygen into the bulk and achieving hard bonding on the surface layer, the sample has uniform states over the entire region, with a much wider depletion region at the GB. Therefore, the carrier transport of the 60 s sample depends considerably on the GB.

3.3. Time-resolved photocurrent with on/off control of ultraviolet light

For a more detailed study concerning carrier transport behavior, we measured the time-resolved photocurrent with on/off control of the UV light. In Fig. 4(a), it can be seen that, once the UV light was turned on, there was an early increase in the photocurrent rate in all samples until point A (blue dashed line). This appeared to depend on the number of oxygen-deficient sites regardless of GB, which is also shown in the inset of Fig. 4(a). The attenuated GB effect under UV light is attributed to the significantly increased carrier concentration in the ZnO nanofilm, which raises the Fermi-level and, as a result, reduces the influence of GB on carrier transport. The dependence of the early increase in rate with the density of the oxygen vacancies is associated with their adsorption/desorption processes. To understand this in more detail, see the diagram of the adsorption/desorption processes in Fig. 4(b). Due to the non-stoichiometry of the ZnO nanofilm, oxygen atoms in the surface layer can more easily be released to the ambient air than oxygen atoms in the bulk. Therefore, the surface layer has a higher density of oxygen vacancies, which leads to higher electron density in the surface than in the bulk. Under ambient air, as mentioned before, oxygen molecules adsorb to the surface layer, forming negatively charged oxygen ions ($O_2(g) + e^- \rightarrow O_2^-(ad)$). This introduces energy-band bending in the surface layer due to the generation of relative electric fields. As a result, owing to its depletion width (DW_S), the conducting path (CW_B) becomes narrower. Under illumination by UV light, photo-excited electron–hole pairs in the DW_S are separated due to the energy-band bending. Consequently, the separated holes move to the surface layer through the inclined valence band and desorb the adsorbed oxygen ions ($h^+ + O_2^-(ad) \rightarrow O_2(g)$), which reduces the DW_S and increases the CW_B. At the same time, the separated electrons contribute to carrier transport. Furthermore, the density of the defect states can increase the gain in MSM-type devices until the defect states are affected by the increased carrier density. (Herein, the gain is defined as the ratio of the number of

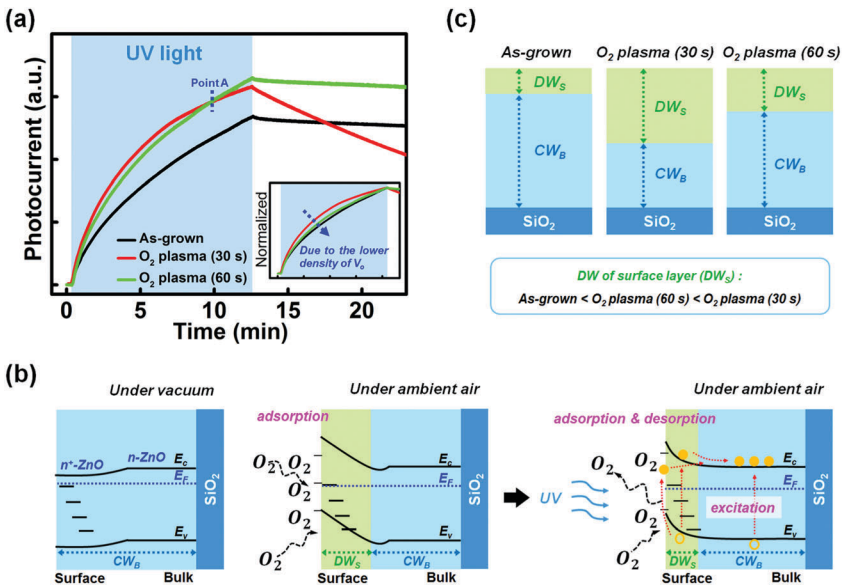

Fig. 4 Time-resolved photocurrents: (a) with on/off control of UV light (wavelength 355 nm, intensity 11.5 mW cm^{-2}) at 0.3 V bias voltage. The normalized inset shows that the early increase rate in the photocurrent depends on the density of oxygen vacancies in the surface layer. The schematic energy band diagrams (b) show the mechanism of adsorption and desorption processes of oxygen molecules in the ZnO nanofilm under on/off control of UV light. DW_S and CW_B mean the depletion width of surface band bending, and the width of the conducting path in the bulk, respectively. The schematic structure (c) presents the relative magnitude of DW_S and CW_B.

electrons collected per unit time, to the number of photons absorbed per unit time.) Therefore, due to the different densities of defect states causing their DW_S and CW_B, as shown in Fig. 4(c), the early rate of increase in their amount was determined as indicated by the measured data in Fig. 4(a). If continuously illuminated by a sufficiently high intensity of UV light, the rates of adsorption and desorption processes could reach an equilibrium state with a dependence on the density of oxygen molecules in the ambient air. Also, in this condition, and if there were no gain due to the defect states being fully saturated by the increased number of electrons, then the amount of photocurrent could rely on the quality of crystallinity.

Once the light was turned off, long persistent conductivities were observed, as shown in Fig. 5. The entire photo response curves can be divided largely into two-part decay mechanisms. In this regard, interestingly, we confirmed a noticeable distinction in the decay curves between the samples of 30 s and 60 s. The initial part of the decay in the 30 s sample (left red arrow) had a fast exponential decrease, and that in the 60 s sample (left green arrow) had a slow inverse-exponential decrease. In contrast, the second part of the decay in the 30 s sample (right red arrow) had a very slow decay curve, and that of the 60 s sample (right green arrow) had a relatively fast exponential decrease. More notably, initially inverse-exponential decay curves in the 60 s and as-grown samples (dashed orange ellipse) appeared, which had not been observed in prior reports (to the best of our knowledge) concerning the persistent photoconductivity of ZnO. The inverse-exponential decay implies that there exists a completely different mechanism against an exponential decay function, in relation to the adsorption/desorption process.

3.4. Carrier transport behaviors depending on the two orthogonally directional energy bands

Regarding the distinct decay curves between the 30 s and 60 s samples, we confirmed that they should be attributed to a correlation between two orthogonally directional energy bands, as shown in the schematic diagrams of Fig. 6(a). As it were, two types of depletion width (DW) exist in the ZnO nanofilm: one is the DW_S of the surface layer due to the surface band bending (in the out-of-plane direction), and the other is the DW_G of GB (in-plane direction). Thus, the 30 s sample exhibits a large DW_S in the out-of-plane and a small DW_G in the in-plane direction, whereas the 60 s sample has a relatively small DW_S in the out-of-plane direction and a large DW_G in the in-plane direction. As mentioned before, under UV light, the photo-generated electrons raising the Fermi-level mitigated the GB effect for carrier transport in all the samples, so the amount of photocurrent, and the early increase rate, depend entirely on the surface band bending resulting from the surface defect states, as shown in Fig. 6(b). After turning off the light, the 30 s sample presenting the initially fast exponential decay, and the subsequent long persistent conductivity, is attributed to the large surface band bending in the surface layer with negligible small DW_G. That is, the carrier transport channel width is largely affected by the surface band bending due to its wide DW_S, which causes initially fast increase and decay times. In the case of its second long decay curve, this is also caused by the large surface band bending because the deep region of oxygen-deficient sites has difficulty interacting rapidly with oxygen in the air. This induces a long, slow adsorption process. In the case of the 60 s and as-grown samples, a wide DW_G and narrow DW_S exist, compared with the 30 s sample. In this condition, inter-grain mobility in the 60 s and as-grown samples could play a crucial role in carrier transport. The intra-grain mobility (μ_{gb})[28] across the grain barriers is dominated by thermionic emission as $\mu_{gb} = \left(qL/\sqrt{2\pi m^* k_B T}\right)\exp(-\varphi_B/k_B T)$, where φ_B is the barrier height of GB, k_B is the Boltzmann constant, L and m^* are an effective grain size and the electron effective mass, respectively. From the formula, it can be seen that the mobility (μ_{gb}) can be substantially reduced by a small increase in the barrier height (φ_B)[29] due to the exponential function. Furthermore, because the barrier height as an activation energy for carrier transport can be presented as $\varphi_B = qN_s^2/8\varepsilon_0\varepsilon_r n$, where N_s is the density of acceptor at the GB and n is carrier concentration, the small increase in adsorbed charges (N_s) at the GB already formed during exposure to oxygen plasma in our experiments has an extreme effect on the mobility because φ_B is also proportional to the square of N_s. Therefore, when turning off the UV light, the carrier transport of the residual photo-generated carrier in the 60 s sample exhibiting the largest DW_G is significantly influenced at a certain time (blue circle and blue dashed arrow), exhibiting a certain concentration of carrier that is blocked by the electrical barrier of GB, which caused the initially unexpected inverse-exponential decay. If there were no GB effect in the 60 s and as-grown samples, only long exponential decay curves would be observed, as shown by the dashed lines in Fig. 6(b), which are only related by their surface band bending in the surface layer. However, in practice, as shown in our observed photoresponse data in Fig. 5, the persistent photoconductivity during the decay time was blocked by GB. Ultimately, through an understanding of the correlation

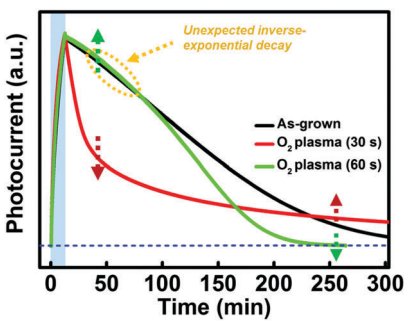

Fig. 5 Time-resolved photocurrents with on/off control of UV light (wavelength 355 nm, intensity 11.5 mW cm^{-2}) at 0.3 V bias voltage, showing a normalized photoresponse graph in the overall region. The sky-blue box indicates the portion with UV light turned on. The horizontal blue dashed line indicates a region of zero current. The falling curves can be divided into a two-part decay mechanism. In particular, the samples of 30 s and 60 s appear to have contrasting decay curves, as indicated by the dashed arrows (green, red). Furthermore, the 60 s and the as-grown samples present an unexpected inverse-exponential decay curve (gold dashed ellipse), which means that there are completely different decay processes against the adsorption process of oxygen molecules.

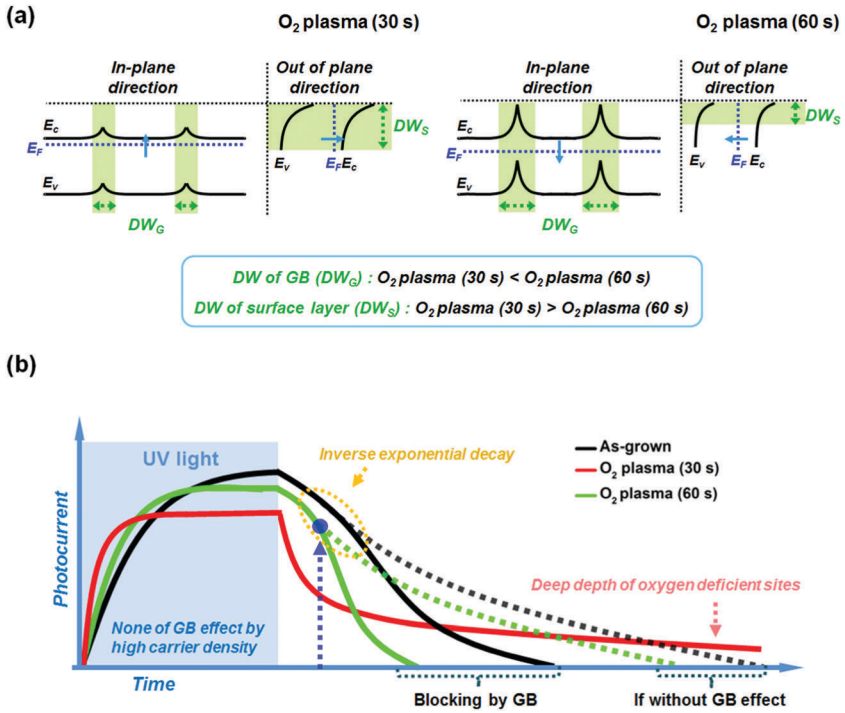

Fig. 6 Schematic diagrams of (a) energy band structures in the 30 s and 60 s ZnO nanofilms show the two orthogonally directional energy bands such as grain boundary (in-plane direction) and surface band bending (out-of-plane direction) in the surface layer. (b) Photoresponse curves with on/off UV light display their carrier transport behaviors, depending on the two orthogonally directional energy bands. Without the GB effect in the 60 s and the as-grown samples, the decay curve would appear as the dashed green and black decay curves without the early inverse-exponential decay. However, in practice, due to the GB effect, the entire decay curves shorten with the appearance of the early inverse-exponential decay. The time position of the blue circle could be the point at which GB influences the carrier transport. Undoubtedly, the position could depend on the relation between the carrier concentration and the electrical barrier height of GB.

between the two types of depletion width resulting from the two orthogonally directional energy band structures, we ascertained the carrier transport behaviors in the ZnO nanofilm. Moreover, we confirmed that the GB effect, modulated by oxygen plasma in the ZnO nanofilm, can block the persistent conductivity with reducing dark current.

4. Conclusions

In summary, we demonstrated the mechanisms of carrier transport behaviors in ZnO nanofilm treated with oxygen plasma. In spite of the short exposure times (30 s and 60 s) to the plasma, the ZnO nanofilms were strongly influenced by ion bombardment and the densification effects due to the nanofilm thickness and the high density of the grain boundary. The resulting carrier transport behaviors were analyzed by understanding the two orthogonally directional energy band structures (grain boundary and surface band bending in the surface layer). By comprehending carrier transport behavior depending on the correlation between the two types of band structures, effective engineering of carrier transport in the oxide semiconductor nanofilm could be possible. Therefore, we believe that our study could be very informative for scientists and engineers researching nanostructured oxide–semiconductors for various functional devices.

Acknowledgements

W. S. Chang acknowledges financial support by the Center for Advanced Soft-Electronics funded by the Ministry of Science, ICT and Future Planning (CASE-2012M3A6A5055728), Korea, and the Basic Research Fund of Korea Institute of Machinery & Materials (SC1170). S.-Mo. Lee acknowledges the financial support from the R&D Convergence Program of MSIP (Ministry of Science, ICT and Future Planning) and NST (National Research Council of Science & Technology) of Republic of Korea (Grant CAP-13-2-ETRI), and the internal research program of Korea Institute of Machinery and Materials (SC1090).

References

1 K. Song, J. Noh, T. Jun, Y. Jung, H. Y. Kang and J. Moon, *Adv. Mater.*, 2010, **22**, 4308–4312.
2 S. Lee, S. Bang, J. Park, S. Park, W. Jeong and H. Jeon, *Phys. Status Solidi A*, 2010, **207**, 1845–1849.
3 X. L. Chen, F. Wang, X. H. Geng, D. K. Zhang, C. C. Wei, X. D. Zhang and Y. Zhao, *Mater. Res. Bull.*, 2012, **47**, 2008–2011.
4 J. C. Wang, W. T. Weng, M. Y. Tsai, M. K. Lee, S. F. Horng, T. P. Perng, C. C. Kei, C. C. Yu and H. F. Meng, *J. Mater. Chem.*, 2010, **20**, 862–866.
5 Y. L. Wang, H. S. Kim, D. P. Norton, S. J. Pearton and F. Ren, *Appl. Phys. Lett.*, 2008, **92**, 112101.

6 C. Park, J. Lee, H. M. So and W. S. Chang, *J. Mater. Chem. C*, 2015, **3**, 2737–2743.
7 M. Liu and H. K. Kim, *Appl. Phys. Lett.*, 2004, **84**, 173–175.
8 A. Umar, M. M. Rahman, S. H. Kim and Y. B. Hahn, *Chem. Commun.*, 2008, 166–168.
9 S. J. Chang, T. J. Hsueh, C. L. Hsu, Y. R. Lin, I. C. Chen and B. R. Huang, *Nanotechnology*, 2008, **19**, 095505.
10 Ü. Özgür, Y. I. Alivov, C. Liu, A. Teke, M. Reshchikov, S. Doğan, V. Avrutin, S.-J. Cho and H. Morkoc, *J. Appl. Phys.*, 2005, **98**, 041301.
11 C. Park, J. Lee and W. S. Chang, *J. Phys. Chem. C*, 2015, **119**, 16984–16990.
12 H. W. Ra, R. Khan, J. T. Kim, B. R. Kang, K. H. Bai and Y. H. Im, *Mater. Lett.*, 2009, **63**, 2516–2519.
13 H. W. Ra and Y. H. Im, *Nanotechnology*, 2008, **19**, 485710.
14 S. Jiang, Z. Ren, S. Gong, S. Yin, Y. Yu, X. Li, G. Xu, G. Shen and G. Han, *Appl. Surf. Sci.*, 2014, **289**, 252–256.
15 C. J. Barnett, O. Kryvchenkova, N. A. Smith, L. Kelleher, T. G. Maffeis and R. J. Cobley, *Nanotechnology*, 2015, **26**, 415701.
16 Y. L. Lee, S. F. Chen, C. L. Ho and M. C. Wu, *ECS J. Solid State Sci. Technol.*, 2013, **2**, P316–P320.
17 S. A. Studenikin, N. Golego and M. Cocivera, *J. Appl. Phys.*, 2000, **87**, 2413–2421.
18 S. M. George, *Chem. Rev.*, 2009, **110**, 111–131.
19 C. Park, H. M. So, H. J. Jeong, M. S. Jeong, E. Pippel, W. S. Chang and S. M. Lee, *ACS Appl. Mater. Interfaces*, 2014, **6**, 16243–16248.
20 T. Singh, T. Lehnen, T. Leuning, D. Sahu and S. Mathur, *Appl. Surf. Sci.*, 2014, **289**, 27–32.
21 A. Kolmakov, Y. Zhang, G. Cheng and M. Moskovits, *Adv. Mater.*, 2003, **15**, 997–1000.
22 X. Li, Y. Wang, W. Liu, G. Jiang and C. Zhu, *Mater. Lett.*, 2012, **85**, 25–28.
23 F. Yi, Y. Huang, Z. Zhang, Q. Zhang and Y. Zhang, *Opt. Mater.*, 2013, **35**, 1532–1537.
24 Y. Chen, D. M. Bagnall, H. J. Koh, K. T. Park, K. Hiraga, Z. Zhu and T. Yao, *J. Appl. Phys.*, 1998, **84**, 3912–3918.
25 N. Huby, S. Ferrari, E. Guziewicz, M. Godlewski and V. Osinniy, *Appl. Phys. Lett.*, 2008, **92**, 3502.
26 D. A. Gulino, L. A. Kren and T. M. Dever, *Thin Solid Films*, 1990, **188**, 237–246.
27 A. C. S. Sabioni, M. J. F. Ramos and W. B. Ferraz, *Mater. Res.*, 2003, **6**, 173–178.
28 A. T. Vai, V. L. Kuznetsov, J. R. Dilworth and P. P. Edwards, *J. Mater. Chem. C*, 2014, **2**, 9643–9652.
29 R. S. Bisht, R. R. Ghimire and A. K. Raychaudhuri, *J. Phys. Chem. C*, 2015, **119**, 27813–27820.